Cite as: Brett, R.C., Russell, J.K., Andrews, G.D.M., Jones, T.J., 2015. The ascent of kimberlite: Insights from olivine. Earth and Planetary Science Letters 424, 119–131. https://doi.org/10.1016/j.epsl.2015.05.024

The Ascent of Kimberlite: Insights from Olivine

R.C. Brett[1,2]*

J.K. Russell[1]

G.D.M. Andrews[1,3]

&

T.J. Jones[4]

[1]Volcanology & Petrology Laboratory, Department of Earth & Ocean Sciences, The University of British Columbia, Vancouver, British Columbia, Canada, V6T 1Z4
[2]Rio Tinto Exploration Canada Inc. Vancouver, British Columbia, Canada, V6C 1S4
[3]Department of Geosciences, California State University Bakersfield, Bakersfield, California, USA, 93311
[4]Department of Earth Sciences, Durham University, South Road, Durham, DH1 3LE, UK

Earth and Planetary Science Letters

Typeset, published version: https://doi.org/10.1016/j.epsl.2015.05.024

*Corresponding Author:
Curtis Brett [Curtis.Brett@riotinto.com]
Phone: +1(604)762-6650
Fax: +1(604)696-3401

Typeset, published version: https://doi.org/10.1016/j.epsl.2015.05.024

Abstract

Olivine xenocrysts are ubiquitous in kimberlite deposits worldwide and derive from the disaggregation of mantle-derived peridotitic xenoliths. Here, we provide descriptions of textural features in xenocrystic olivine from kimberlite deposits at the Diavik Diamond Mine, Canada and at Igwisi Hills volcano, Tanzania. We establish a relative sequence of textural events recorded by olivine during magma ascent through the cratonic mantle lithosphere, including: xenolith disaggregation, decompression fracturing expressed as mineral- and fluid-inclusion-rich sealed and healed cracks, grain size and shape modification by chemical dissolution and abrasion, late-stage crystallization of overgrowths on olivine xenocrysts, and lastly, mechanical milling and rounding of the olivine cargo prior to emplacement. Ascent through the lithosphere operates as a "*kimberlite factory*" wherein progressive upward dyke propagation of the initial carbonatitic melt fractures the overlying mantle to entrain and disaggregate mantle xenoliths. Preferential assimilation of orthopyroxene (Opx) xenocrysts by the silica-undersaturated carbonatitic melt leads to deep-seated exsolution of CO_2-rich fluid generating buoyancy and supporting rapid ascent. Concomitant dissolution of olivine produces irregular-shaped relict grains preserved as cores to most kimberlitic olivine. Multiple generations of decompression cracks in olivine provide evidence for a progression in ambient fluid compositions (e.g., from carbonatitic to silicic) during ascent. Numerical modelling predicts tensile failure of xenoliths (disaggregation) and olivine (cracks) over ascent distances of 2-7 km and 15-25 km, respectively, at velocities of 0.1 to >4 m s^{-1}. Efficient assimilation of Opx during ascent results in a silica-enriched, olivine-saturated *kimberlitic* melt (i.e. SiO_2 > 20 wt.%) that crystallizes overgrowths on partially digested and abraded olivine xenocrysts. Olivine saturation is constrained to occur at pressures <1 GPa; an absence of decompression cracks within olivine overgrowths suggests depths < 25 km. Late stage (< 25 km) resurfacing and reshaping of olivine by particle-particle milling is indicative of turbulent flow conditions within a fully fluidized, gas-charged, crystal-rich magma.

Typeset, published version: https://doi.org/10.1016/j.epsl.2015.05.024

1. Introduction

Kimberlite magmas derive from deep (≥ 200 km) mantle sources and transport substantial loads (> 25 vol. %) of dense, mantle-derived xenoliths and xenocrysts from the base of the mantle lithosphere to the Earth's surface. They are found almost exclusively within Archean cratons and are of particular interest because they are the deepest-sourced terrestrial magmas, are the major source rock of natural diamond, and carry xenoliths which inform on the petrology, structural state, and temperature of the deep cratonic mantle lithosphere.

The rapid transport of kimberlite through ~150-200 km of cool cratonic mantle lithosphere has been discussed by McGetchin and Ullrich (1973), Sparks et al. (2006; 2013), Wilson and Head (2007) and Kavanagh and Sparks (2009). Most kimberlite ascent models involve the propagation of a volatile-rich magma-filled crack upward through the mantle lithosphere. The exsolution and expansion of a fluid phase creates pressure gradients (100-300 MPa, Lensky et al. 2006; 70 MPa, Wilson and Head, 2007; Sparks, 2013) large enough to induce crack propagation within the mantle and the buoyancy needed to support continuous and rapid ascent. Russell et al. (2012; 2013) suggested a mechanism for the deep-seated exsolution of CO_2-rich fluids; carbonatitic magmas enter and ascend the cratonic mantle lithosphere and sample and disaggregate peridotite xenoliths. Orthopyroxene is assimilated preferentially over other mantle mineral phases (Mitchell, 1973) causing an increase in the melt's SiO_2 content, a drop in CO_2 solubility, and the spontaneous exsolution of a CO_2-dominated fluid phase (Brey and Ryabchikov, 1994; Brooker et al., 2011; Russell et al., 2012; Sparks 2013; Moussallem et al., 2014). This provides a continuous decrease in density, an increase in buoyancy and an accelerating ascent even with increasing loads of dense mantle cargo. Despite these recent advances in our understanding of kimberlite origins and transport (Wilson and Head, 2007; Sparks et al., 2006; Kavanagh and Sparks, 2009; Russell et al., 2012, 2013), many physical

aspects of kimberlite ascent, and their time scales, remain unresolved.

Olivine is ubiquitous and volumetrically the most important constituent in kimberlite; it mainly derives from disaggregated mantle-derived peridotite or dunite (Clement et al., 1984; Mitchell, 1986; Arndt, 2006; Moss et al. 2010). Here, we describe a diverse array of textural features in kimberlitic olivine and build on previous studies of sizes, shapes and surfaces of kimberlitic olivine (e.g., Brett et al., 2009; Jones et al., 2014; Moss et al., 2009; Jerram et al., 2009). The majority of features within xenocrystic olivine result from syn- to post-entrainment processes operating during magma ascent, including: grain size and shape modification, healed and sealed fractures, late-stage crystallization of overgrowths, and very-late resurfacing and reshaping (rounding) of the olivine cargo by mechanical milling.

We establish the relative timing of each textural element and relate the individual textural features to specific physical and chemical processes attending kimberlite ascent. These observations, combined with modelling of the decompression-driven, tensile failure of xenoliths and olivine crystals, lead to an integrated model for the physical transport of kimberlite magmas. We propose that ascent via upward dyke propagation through cratonic mantle lithosphere operates as a *kimberlite factory,* whereby parental carbonatitic magmas are progressively converted to kimberlite (e.g., Russell et al. 2012; 2013; Bussweiler et al. 2015). The sequence of textural elements recorded by kimberlite-hosted olivine inform directly on the physical mechanisms, chemical conditions, and timescales of kimberlite ascent.

2. Previous studies of kimberlitic olivine

Olivine has been used as a means to constrain the origins, composition, transport, and eruption of kimberlite in numerous studies (Fedortchouk and Canil, 2004; Arndt et al., 2006; 2010; Kamenetsky et al., 2008; Brett et al., 2009; Jerram et al. 2009; Moss et al. 2010; Arndt et

al., 2010; Pilbeam et al., 2013; Jones et al., 2014; Bussweiler et al., 2015). Arndt et al. (2010) propose a three-fold classification of kimberlitic olivine, which we adopt here: (1) a dominant population of medium to coarse-grained (> 1 mm), rounded to sub-rounded grains (Figs. 1A,B); (2) fine-grained (< 1 mm) euhedral to subhedral olivine crystals (Figs. 1C,D); and (3) faceted, strain-free tablets (<0.01 - 1 mm) of olivine or neoblasts (Figs. 1E,F). Recent work has established that olivine in kimberlite has a continuous grain size distribution spanning <0.01 mm to 5 cm in diameter (e.g., Jerram et al., 2009; Moss et al., 2010). Olivine grain morphology gradually changes with grain size from euhedral (fine grained) to anhedral or rounded (coarse grained) (e.g., Sobolev et al., 2015).

Cores of olivine macrocrysts show intense internal micro-fracturing, undulose extinction, deformation bands, and commonly contain mineral inclusions (e.g., garnet, clinopyroxene) indicative of lower lithospheric mantle conditions (Reid et al., 1975; Kamenetsky et al., 2008; Bussweiler et al., 2015). The compositions of the cores also indicate a peridotitic mantle origin; they have high Ni contents (3000 – 4000 ppm NiO), low CaO (<1000 ppm) and varying Mg # (0.88 – 0.93; Griffin et al., 2003; Kamenetsky et al., 2008; Brett et al., 2009). Bussweiler et al. (2015) argue, on the basis of detailed chemical study of olivine cores, and the ubiquitous presence of peridotitic minerals (garnet, spinel, clinopyroxene), that kimberlite had traversed and sampled peridotitic mantle at all depths. Elevated Mg-rich (i.e. shallower, depleted mantle) core compositions tend to be more angular relative to more rounded, higher Fe content cores (i.e. deeper, fertile mantle). They ascribed these differences in xenocrystic olivine core shape to longer transit times offering greater opportunities for mineral dissolution.

The cores to all kimberlitic olivine commonly have thin (<150 micron), chemically distinct rims; the core-rim interface can also be marked by abundant mineral and fluid inclusions (Fig. 1; Kamenetsky et al., 2008; 2012; Brett et al., 2009, Arndt et al., 2010; Pilbeam et al.,

2013). The rims are characterized by lower NiO, higher CaO contents and, commonly, a lower and narrower range of Mg# (Fedortchouk and Canil, 2004; Arndt et al., 2006; Kamenetsky et al., 2008; Brett et al., 2009; Bussweiler et al., 2015). The core to rim zoning suggests the rims are overgrowths representing new crystallization of the melt onto pre-existing xenocrystic cores of olivine (Fedortchouk and Canil 2004; Arndt et al. 2006; Kamenetsky et al. 2008; Brett et al. 2009; Sobolev et al., 2015). The exterior margins of the olivine overgrowths commonly have an even thinner rim (~2 microns) characterized by higher forsterite (Fo_{96}) and CaO (< 2 wt.%) contents and lower NiO (<1000 – 1500 ppm; Fedortchouk and Canil, 2004; Brett et al., 2009; Bussweiler et al., 2015). These compositions have been ascribed to changing oxidation conditions, perhaps due to elevated H_2O contents or co-crystallization of additional phases (e.g. chromite; Bussweiler et al., 2015).

Smaller (< 50 μm), euhedral olivine crystals within the groundmass have similar compositions to the overgrowths suggesting that overgrowths and phenocrysts represent concomitant crystallization of the kimberlite melt (Fedortchouk and Canil, 2004; Arndt et al., 2006; Kamenetsky et al., 2008; Brett et al., 2009). The total volume of olivine crystallized during ascent is thought to vary between ~5-20% (Brett et al., 2009; Patterson et al., 2009; Arndt et al., 2010; Bussweiler et al., 2015) which is lower than original estimates (e.g., ~25%; Mitchell, 1986). Trace element compositions reported for olivine overgrowths and olivine phenocrysts show enrichment in Ca, Mn, Cr, Ti, Al, P, V, Sc, Nb, Ga and Zr, which is consistent with simultaneous olivine crystallization and orthopyroxene (Opx) dissolution (Bussweiler et al., 2015).

Deformation bands (Fig. 1E), undulose extinction, and sub-grain development (Fig. 1E-F) characterize many olivine xenocrysts. These strain indicators populate cores of olivine xenocrysts but are absent in olivine overgrowths and phenocrysts; this suggests that deformation

predates xenolith entrainment (Arndt et al., 2010). At high temperature and in low stress environments, the highly strained portions of olivine will recrystallize or anneal on relatively short timescales (Mercier, 1979) to form tablet-shaped neoblasts. In kimberlite, the olivine neoblasts typically have compositions similar to peridotitic olivine, indicating they represent recrystallization of originally highly-strained xenocrysts (e.g., Arndt et al., 2006; 2010; Brett et al., 2009).

3. Sample Suite

Our samples derive from hypabyssal kimberlite dykes from four pipes (A154N, A154S, A418, A21) at Diavik Diamond Mine (DDM), N.W.T, Canada (Brett et al., 2009; Moss et al., 2009) and from the Quaternary Igwisi Hills kimberlite volcanoes (IHV) in Tanzania (Reid et al., 1975; Dawson 1994; Brown et al., 2012; Jones et al., 2014). Samples were selected on the basis of their young ages (54 Ma and 10 ka, respectively), their high olivine contents, and the relative absence of post-emplacement alteration (see Figs. 1-4). Diavik samples contain 40-50 vol. % olivine and have a groundmass of monticellite, apatite and oxides (perovskite, spinel-ulvöspinel, chromite) enclosed by carbonate or carbonate and serpentine (cf. Moss et al., 2009 and Brett et al., 2009). IHV samples are from coherent lavas containing abundant, fresh, distinctively rounded, ellipsoidal olivine xenocrysts. Additional detailed mineralogical and geochemical descriptions can be found in Reid et al. (1975), Dawson (1994), and Brown et al. (2012).

4. Descriptive properties of kimberlitic olivine

The most distinctive features of kimberlitic olivine, in addition to their modal abundance, are their internal petrographic features, shapes and geochemistry. Olivine separated from

samples of DDM and IHV kimberlite share a common set of properties and textures that are described here.

4.1 Olivine overgrowths

All olivine grains in DDM and IHV kimberlite samples have overgrowths of magmatic olivine on irregular cores of xenocrystic olivine (Fig. 1A-D). The relatively thin overgrowths on the larger xenocrysts cause little change in grain shape (Fig. 1A-B), whilst smaller xenocrysts commonly develop subhedral to euhedral overgrowths (Fig. 1C-D). In the DDM and IHV samples, the interface between the olivine overgrowths and their xenocrystic cores is populated by trapped fluid, mineral and melt inclusions, and coincides with an abrupt change in the chemical composition of the olivine (Reid et al., 1975; Brett et al., 2009). The fluid and melt inclusions occur as discontinuous trails parallel to the margins of the anhedral xenocryst cores (Fig. 1). Small inclusions of Mg-chromite and spinel are also trapped at the interface and appear to increase in size towards the margin of the olivine grain (Fig. 1A-D).

4.2 Mineral- and fluid-filled fractures

The anhedral cores of kimberlitic olivine grains commonly host networks of sub-parallel micro-cracks (Fig. 2A). The olivine-hosted fractures fall into two broad categories based on their infill and geometry: 1) *sealed* cracks comprise sets of subparallel, near-planar cracks of varying aperture (<5 μm) that are filled by carbonate and minor oxide inclusions; and 2) *healed* cracks comprise numerous planar to curviplanar cracks expressed as discontinuous trails of fluid and mineral inclusions. The latter have features characteristic of crack-healing processes (Fig. 3; cf. Roedder, 1984; Smith and Evans, 1984). In these samples, the population density of sealed cracks is substantially less than for healed cracks (Fig. 2 *vs*. Fig. 3).

Typeset, published version: https://doi.org/10.1016/j.epsl.2015.05.024

196

197 *4.2.1 Sealed cracks*

198 Figure 2 illustrates the main properties of the sealed cracks found in olivine xenocrysts
199 from DDM and IHV. In cross-section sealed cracks are expressed as near linear, planar to
200 undulating, continuous and discontinuous, ≤5 μm thick segments and patches of elongate
201 carbonate (Fig. 2A-B). Commonly, the carbonate-filled sealant is Sr-Ba-rich calcite enclosing
202 minor inclusions of Mg-chromite with ulvöspinel overgrowths (e.g. Fig. 2B). Crack sealing
203 occurs when ambient fluids are drawn into the void space created by a mineral fracturing event
204 allowing for crystallization of new material (Fig. 2A-D). The fluid precipitates minerals that
205 cement and, thereby, seal the fractures. The sealed cracks do not extend to the outer margins of
206 the olivine grains. Rather, they terminate at the interface between the anhedral olivine xenocryst
207 core and its overgrowth (Fig. 2C).

208

209 *4.2.2 Healed cracks*

210 There is abundant textural evidence for later micro-fracturing events that are expressed as
211 partially to fully healed cracks (cf. Roedder, 1984; Smith and Evans, 1984). Typical examples of
212 the intense networks of healed cracks within olivine from the Diavik and Igwisi Hills kimberlites
213 are shown in the insets to Figures 3A and 3B, respectively. The healed fractures form networks
214 of sub-parallel cracks and are much more numerous than the sealed cracks (Fig. 3A-B insets).

215 The healed cracks, rather than filled by carbonate, are preserved as trails of brownish-
216 coloured, spherical to droplet-shaped melt and fluid inclusions (Fig. 3A-D). Compared to the
217 inclusions trapped at the overgrowth interface (Figs. 1, 2C, 3A), inclusions within the healed
218 cracks are more abundant and exhibit a spectrum of inclusion morphologies (Fig. 3A-B;
219 Roedder, 1984). Partially healed cracks are preserved as connected (Fig. 3C) or isolated tubules

(Fig. 3D). The elongate tubules have a maximum width of 5 μm and can be 10 times as long. Fully healed cracks are preserved as trails of roundish inclusions or inclusions showing negative crystal forms (Fig. 3E). Spherical inclusions are typically < 5 μm in diameter, have transparent centers and dark brown rims.

The healed cracks can extend across almost an entire olivine grain but, as observed for sealed cracks, they terminate at the interface between the olivine core and its overgrowth (Fig. 3A). Furthermore, in all cases the healed cracks overprint the sealed cracks (Fig. 3F-G). Similar to the formation of sealed cracks, healing requires external fluids to fill the void space created by micro-fracturing of the mineral. Following entrapment of the fluid, dissolution and crystallization of the host mineral (i.e. olivine) reduces asperities on the crack surface (Roedder, 1984, Bodnar, 2003). This process decreases fluid volume by "necking down" and is preserved as discontinuous trails of irregular to spherical shaped fluid or melt inclusions (Fig. 3C-D) enclosed by the newly crystallized host mineral (Fig. 3F). If this maturation process goes to completion the original fluid-filled fracture plane disappears to be manifest only by numerous isolated spherical or negative-crystal shaped (Fig. 3E) fluid inclusions (Bodnar, 2003). The healing rates of these cracks can be on a time scale of hours to several days, and depends on crack geometry, temperature, and fluid composition (Wanamaker et al., 1990).

4.3 Olivine shapes and surfaces

Kimberlite contains abundant olivine grains that are rounded and ellipsoidal (Mitchell, 1973, 1986; Reid et al., 1975; Jones et al., 2014). Our analysis of the textures and shapes of the DDM and IHV kimberlitic olivine is based on petrographic study of polished thin sections (Figs. 4A, 4B) and scanning electron microscopy (SEM; Fig. 4C-D). The SEM study used olivine grains carefully separated from coherent kimberlite by hand to preserve the exterior grain

surfaces. SEM grain mounts inform on the three-dimensional shapes and surfaces of individual olivine grains.

In two-dimensions, olivine macrocrysts are typically well-rounded and range in cross-sectional shape from circular to elliptical (i.e. aspect ratios 1:1 to 2:1; Fig. 4A-B). Under SEM olivine grains are uniformly well-rounded and have irregular ovoidal three-dimensional shapes. The exterior surfaces of these rounded olivine grains are texturally distinct and appear "*flakey-smooth*" wherein, at the mm-scale, the surfaces appear continuous and smooth (Fig. 4C-D) but at higher magnification are flaked and layered. In detail, the surfaces are rough, pitted and highly complex (Fig. 4E) rather than smooth or polished, and have substantial relief across the entirety of the olivine grain (cf. Jones et al. 2014).

For comparative purposes, we show a high magnification view of olivine from a mantle-derived peridotite xenolith (Fig. 4F). The shape and surface of the mineral grain are typical of olivine that populates coarse-grained equilibrium textured mantle peridotite. The grain surfaces are smooth at the micron scale and are virtually featureless; facets represent the interlocking of neighboring olivine grains forming ~120^{o} grain boundaries typical of texturally equilibrated mantle (or metamorphic) rocks

The surface properties of mantle-hosted olivine (Fig. 4F) are strikingly different from the surfaces of olivine macrocrysts recovered from kimberlite (Fig. 4A- E). Despite their regular ovoidal shapes, kimberlitic olivine surfaces are demonstrably rougher and are substantially more complex. Their surfaces exhibit a penetrative flaking and curving micro-ridges that result from pitting and chipping of the exterior surface. Figure 4F illustrates the three-dimensional shapes and the surface textures of the olivine grains that are initially released to the kimberlite melt. It is clear that a pervasive and efficient size, shape and surface modifying process must operate during kimberlite ascent to create these differences (e.g., Fig. 4E *vs*. 4F).

5. First Order Interpretation of Timing Relationships

The textural relationships, described above, establish a relative sequence of events occurring once peridotitic mantle xenoliths are within the rising magma. The xenoliths are disaggregated releasing large populations of euhedral to subhedral olivine xenocrysts and other peridotitic minerals. All peridotitic minerals released to the magma are out of equilibrium and react and dissolve in the strongly silica-undersaturated melt at rates depending on their composition (e.g., Luth, 2009; Brett et al., 2009; Russell et al., 2012; 2013). Chemical dissolution produces the irregular, embayed, anhedral shapes found preserved as cores to xenocrystic and phenocrystic olivines (cf. Fedortchouk and Canil., 2004; Kamenetsky et al., 2008; Brett et al., 2009; Pilbeam et al., 2013; Bussweiler et al., 2015; Sobolev et al., 2015).

The partially-digested olivine xenocrysts develop internal fractures that fill and seal with carbonate rich fluid; these sealed fractures are cross-cut by a later set of healed fractures that are filled by a more silicic, and possibly more hydrous magma, capable of crystallizing/precipitating olivine and no longer crystallizing carbonate. The implication is that the olivine xenocrysts record two different generations of cracks that are filled with intrinsically different material and both predate crystallization of the olivine overgrowths. The earlier 'fill' material crystallized as carbonate whilst the later mineral fracturing event captures fluid/material more amendable to annealing of the host olivine. This suggests that at the time of formation of the healed cracks the melt was near or at olivine saturation allowing healing of the internally-fractured olivine and trapping mineral/fluid inclusions. The sealed cracks pre-date or are coincident with the olivine saturation event responsible for the olivine overgrowths which cap the sealed cracks (Fig. 2D).

Ultimately, the melt becomes fully saturated with olivine (but not clinopyroxene) allowing crystallization of overgrowths (and phenocrysts) on olivine that traps fluid and mineral

inclusions. The olivine overgrowths result from crystallization of the kimberlitic melt onto exterior surfaces of pre-existing, partially-corroded, irregularly-shaped olivine xenocrysts derived from disaggregated mantle rocks (e.g., peridotite and dunite) (Fedortchouk and Canil 2004, Arndt et al. 2006; Kamenetsky et al. 2009; Brett et al. 2009).

The last textural event is the reshaping and resurfacing of olivine that produces the rounded to ellipsoidal olivine grains and their micro-flaked exterior surfaces. Most previous workers have invoked chemical dissolution to account for the overall shape modification of olivine (e.g., Kamenetsky et al., 2008; Pilbeam et al., 2013). However as developed below, we favour the physical process of mechanical abrasion for this overall transformation of initially subhedral to euhedral shaped mantle olivine into the rounded olivine grains that populate kimberlite. (e.g., Reid et al., 1975; Arndt et al., 2010; Jones et al., 2014).

6. The Kimberlite Factory Model

The model of Russell et al. (2012; 2013) and adapted by (Kamenetsky and Yaxley, 2015) provides a mechanism for deep-seated exsolution of CO_2-rich fluids. They propose that carbonatitic magmas entering the base of the cratonic mantle lithosphere evolve as they transit the cratonic mantle lithosphere to erupt as kimberlite (Fig. 5A). All peridotitic minerals released to the initially strongly silica-undersaturated magma are out of equilibrium and begin to react and dissolve at rates depending on their composition. The key to their model was the preferential assimilation of Opx (the most silica-saturated mantle phase) released to the melt by disaggregation of entrained peridotitic xenoliths (Mitchell, 1973; Luth, 2009; Brett et al., 2009). Assimilation of Opx (and other mantle silicates) causes SiO_2-enrichment of the carbonatitic melt inducing a marked drop in CO_2 solubility, causing spontaneous exsolution of a volatile phase rich in CO_2, and increasing buoyancy (Brey and Ryabchikov, 1994; Brooker et al., 2011; Russell et al., 2012; Sparks 2013; Moussallem et al., 2014; Kamenetsky and Yaxley, 2015).

316 In contrast, Cordier et al., (2015) and Arndt et al. (2010) propose pre- to syn-kimberlite
317 defertilization of peridotitic mantle by carbonatitic melt that removes orthopyroxene to create a
318 more dunitic mantle. Kimberlitic magmas driven by CO_2 exsolution ascend with no further Opx
319 dissolution required. Our observations support a more progressive process involving
320 modification of an ascending carbonatitic magma that continuously entrains, disaggregates, and
321 reacts with lithospheric mantle during ascent.

322 Physically, the ascent of kimberlitic magma comprises a sequence of processes,
323 including: 1) cracking of the overlying mantle lithosphere driven by over-pressures due to rising
324 buoyancy forces in the fluid-saturated dyke; 2) dyke propagation and episodic advance of the
325 fluid-wetted crack tip; 3) sampling and entrainment of mantle wall rocks; 4) ascent of the magma
326 and inflation of a new length of dyke; and 5) elastic recovery and closing up of tail of the
327 kimberlite dyke. These processes are repeated continuously as the rising and chemically evolving
328 magma moves progressively through the mantle lithosphere all the while carrying mantle cargo
329 in the form of xenoliths and xenocrysts (Fig. 5A).

330 We suggest that transport through the mantle represents a *kimberlite factory* (Fig. 5B)
331 wherein buoyant carbonatitic melt that is infiltrating and rising through a brittle, elastic mantle
332 lithosphere is converted to what, ultimately, erupts as kimberlite magma. Kimberlite dykes are
333 notably thin (< 5 m) compared to their lateral widths (10's to 100's on m) and their presumed
334 vertical lengths (100's of m to km's) and, thus, can be effectively modelled as planar sheets (cf.
335 Kavanagh et al. 2011). We see the kimberlite factory as the idealized, elastically-inflated portion
336 of a vertical sheet (dyke) of kimberlite magma (Fig. 5B) consistent with the modelling of
337 Menand and Tait, (2002) and Kavanagh et al. (2006) and as developed and applied by Sparks et
338 al., (2006), Kavanagh et al. (2011), and Sparks, (2013). Using their models, we have calculated
339 the critical widths and lengths of the bulbous head portion of the kimberlite dyke (cf. Menand

and Tait, 2002) for a reasonable range of properties pertinent to kimberlite ascent (Supplementary Appendix A). We suggest that this portion of the dyke is a good candidate for the kimberlite factory wherein the olivine cargo and kimberlite magma inherit many properties during ascent through the cratonic mantle lithosphere (Fig. 5A).

Our calculations are for a range of magma viscosities (25 - 50 Pa s) and magma densities corresponding to variable proportions of xenocrysts and exsolved fluid (Fig. A1). The bulk magma densities define the density contrast ($\Delta\rho$) relative to a lithospheric mantle density of 3300 kg m^{-3}. The critical vertical length of the upper bulbous head varies from 4.5 to 1.5 km for small (~100 kg m^{-3}) and large (500 kg m^{-3}) density contrasts, respectively. The corresponding minimum critical dyke widths vary from 2 to 1 m, respectively, and are consistent with widths of a large number of kimberlite dykes (c.f. Kavanagh et al., 2006). If the system becomes more enriched in exsolved CO_2 (i.e. continued Opx dissolution) or depressurization causes a major expansion of the fluid phase, the density contrast and buoyancy rise substantially and the minimum dimensions (L_c and W_c) for the dyke head may be even smaller (cf. Kavanagh et al., 2006).

We have calculated the magma ascent velocity (U) for buoyancy-driven flow in the dyke geometries described above (cf. Sparks et al., 2006; Supplementary Appendix A). The model ascent velocities are >1 m s^{-1} which, based on the Reynolds numbers for the corresponding dyke widths, support turbulent flow (Supplementary Appendix A). An average velocity of 1 m s^{-1} implies ~40 hours for transit through 150 km of mantle lithosphere. The volume of CO_2-rich fluid will increase during ascent as CO_2-fluid exsolves continuously (assimilation-induced vesiculation) and as pressure decreases causing additional exsolution and fluid expansion. This generates a substantial decrease in density, and a continuous, increase in buoyancy allowing the

363 magma to accelerate to velocities > 10 's of m s^{-1} through the uppermost mantle and crust even as
364 the load of dense mantle cargo increases.
365

366 **7. Decompression cracking during ascent**

367 Textural information recorded by olivine, coupled with the intrinsic properties of this
368 mineral (bulk modulus, viscosity and tensile strength; Table 1), constrains magma ascent rates
369 (Fig. 6). Olivine found in the DDM and IHV kimberlite hosts pervasive sealed and healed cracks
370 indicating repeated failure of olivine prior to eruption. We interpret these as tension cracks
371 resulting from rapid decompression during kimberlite ascent.

372 Kimberlite ascent through the lithosphere subjects the mantle cargo to rapid changes in
373 confining pressure. Decompression by decreasing lithostatic pressure during ascent requires
374 olivine to expand volumetrically. Over long timescales, expansion can be achieved by viscous
375 relaxation involving changes in bond angles and/or bond lengths. Where decompression occurs
376 at rates faster than the mineral's characteristic viscous relaxation rate, internal elastic stresses
377 accumulate. Xenolith disaggregation and cracking of minerals result if internal stresses exceed
378 intrinsic tensile strengths.

379 The competition between the rise of internal elastic stresses due to decompression, and
380 viscous relaxation of these stresses dictates the mineral grain's residual stresses ($\Delta\sigma_R$). Values of
381 $\Delta\sigma_R$ are calculated with Equation 1:

382 $$\Delta\sigma_R = \rho\, g[z_0 - z] - K_T \frac{\rho g}{2\,\eta\, U}[z_0 - z]^2 \qquad (1)$$

383 where K_T is the bulk modulus of olivine, η is Newtonian viscosity of OH-rich olivine, U is the
384 ascent velocity, ρ is density of the mantle lithosphere, and the term $\rho g[z - z_0]$ is the pressure

drop due to ascent (Supplementary Appendix B). Parameter values are given in Table 1. The velocity of the ascending magma dictates the time available for viscous relaxation.

We use Equation 1 to model the stress state ($\Delta\sigma_R$) of OH-rich mantle olivine as a function of transport distance (i.e. decompression) in an ascending magma for a range of ascent velocities (Fig. 6A). These stresses are compared to the tensile strengths of olivine and of coarse and fine-grained peridotite (Fig. 6B). The conditions where xenoliths and olivine fail in tension are marked by the intersection of the residual stress curves (for specific velocities) and the horizontal shaded grey bands (Fig. 6B).

Faster ascent rates dictate less viscous relaxation causing failure at smaller transport distances. Slower ascent allows longer times for viscous relaxation and therefore transport distances before olivine fractures. Any ascent velocity ≥ 1 m s^{-1} is sufficiently rapid to suppress viscous relaxation and the residual stresses are equal to the elastic limiting stresses. At these velocities the internal stresses rise to exceed the tensile strength of olivine after ~15 km of ascent (~4 hours at 1 m s^{-1}); at these velocities the magma would transit 200 km in ~ 2 days. At lower velocities (e.g., 0.1 m s^{-1}), larger transport distances (22 km) are required to generate internal residual stresses exceeding the tensile strength of olivine (Fig. 6B). An average velocity of 0.1 m s^{-1} corresponds to a total transit time for 200 km of 23 days. At lower velocities, viscous relaxation begins to dominate over characteristic transport distances (dashed line, Fig. 6B) and the stress needed to crack olivine is never reached. The recorded decompression induced cracking of olivine macrocrysts sets a minimum ascent velocity of > 0.1 m s^{-1}.

In terms of rock strength, polymineralic rocks are generally weaker by a factor of ~10 than the minerals comprising the rock; coarse-grained rocks are generally weaker than fine-grained rocks. Decompression during ascent causes early disaggregation of peridotitic xenoliths (coarse ones first) and continually releases the suite of mantle-mineral xenocrysts (i.e. olivine,

orthopyroxene, clinopyroxene, garnet) to the melt (Fig. 6B). Coarse-grained peridotite xenoliths begin to disaggregate after a pressure drop of ~100 MPa corresponding to < 5 km of ascent; fine-grained peridotite can withstand decompression up to ~200 MPa (< 10 km ascent). Large ~10 cm diameter xenoliths of coarse to fine grained peridotite are common in kimberlite. However, xenoliths hosting megacrystic-sized olivine are rarely observed in kimberlite suggesting that such xenoliths disaggregate rapidly and very efficiently with relatively small degrees of depressurization. Thus, the crystal cargo is preferentially populated by mantle minerals derived from coarse to very coarse peridotite, whilst a higher proportion of finer-grained peridotites or monomineralic xenoliths are transported intact.

8. Discussion

The schematic model showing the multiphase-flow architecture of the kimberlite factory (Fig. 5B) is expanded to show the linkages between the observed textural properties of kimberlitic olivine and the processes operating during magma ascent (Fig. 7). There are five linked domains within the kimberlite factory where different physical-chemical processes dominate, including: 1) the inflated crack tip, 2) the fluid charged head, 3) a transitional zone, 4) the melt-rich tail, and 5) the relaxed closed dyke (Fig. 7).

The dominant processes associated with each domain are: sampling and disaggregation of mantle wall rocks (No. 1); decompression cracking of olivine (No. 2); partial dissolution of olivine (and other minerals) xenocrysts by carbonatitic melt and partial milling within turbulent flow (No. 2-4); sedimentation and re-entrainment of olivine and mantle xenoliths into melt-dominated magma (No. 4); heterogeneous crystallization of olivine on partially-corroded, anhedral to sub-rounded mechanically-abraded xenocrysts (No. 4); and continued settling of olivine to the gas-depleted tail of the kimberlite (No. 5). The last process involves additional

mechanical milling of the xenocrysts causing the final reshaping and resurfacing of the olivine cargo. This process operates after the magma has reached olivine saturation and we suggest it begins to dominate in the uppermost mantle and crust when the system flashes to a gas dominated, fluidized state.

8.1 Fluidization Processes

Deep-seated production of CO_2-rich fluid (Russell et al., 2012; 2013) allows for segregation of the rising magma, based on buoyancy contrasts, into a fluid-rich head and a solid laden tail of melt (e.g., Vergniolle and Jaupart 1986; Moss et al. 2009). The exsolved fluid phase will decompress more efficiently than the melt, leading to a rapidly rising fluid volume fraction with ascent. As both the volume of the fluid phase and the suspended load increase, there is an ever-increasing tendency for the magma to segregate into a volumetrically dominant, fluid-rich, cap and a trailing body of crystal laden melt (Fig. 7). This results in the upper portion of the factory comprising a turbulent, CO_2-rich fluid-dominated suspension of melt and olivine xenocrysts.

The upward propagation of the magma is facilitated by continued segregation, expansion, and flow of the CO_2-rich fluid phase upward to fill the dyke tip. High over-pressures in the fluid-wetted crack-tip rise to the point that the overlying mantle lithosphere is damaged and, then, fails creating another dyke propagation event (~10-70 MPa; Wilson and Head, 2007). Repeated failure and dyke propagation allows for simultaneous and continual sampling of mantle xenoliths (e.g., Rubin 1995; Lensky et al., 2006; Sparks, 2013). Rapid ascent of the gas-rich head facilitates the break-up of the mantle xenoliths over short (~ 5 km) transport distances by decompression (Fig. 6b) thereby populating the magma with abundant xenocrysts for the entire ascent of kimberlite. Turbulent and fluidizing conditions begin to mill, and partially round

olivine xenocrysts. Liberated orthopyroxene grains (and other silicates) are assimilated by the melt promoting sustained exsolution of a CO_2 dominated fluid phase, providing a larger volume of CO_2-rich fluid to expand in the turbulent fluidized head of the kimberlite factory.

8.2 Fluid Evolution and Sampling

The rapid decompression and accelerating ascent rates attending kimberlite transport cause continuous disaggregation of xenoliths, chemical dissolution of the liberated mantle silicate phases, and concomitant tensile failure of olivine xenocrysts. The decompression attending rapid ascent also causes repetitive cracking of the olivine crystal cargo.

Fluids external to the cracked crystals are efficiently siphoned into cracks because of low wetting angles between the host olivine and carbonatitic melt or CO_2-rich fluid. The carbonate sealed cracks provide evidence of melt being drawn into decompression cracks and precipitating. In this regard, the carbonate-filled sealed cracks strongly support to the hypothesis that all kimberlite magmas originate as carbonatitic-melts (e.g., Russell et al., 2012, 2013; Kamenetsky et al., 2013; Pilbeam et al., 2013; Kamenetsky and Yaxley, 2015; Bussweiler et al. 2015).

Below the turbulent fluid-rich head of the dyke is a transitional flow regime comprising frothy to bubbly melt (grey region; Fig. 7) that is followed by a lagging tail of magma laden with a dense cargo of intact xenoliths and modified olivine xenocrysts. The trailing domain of ascending melt collects settling olivine xenocrysts and continues to supply exsolved fluid to the overlying fluid-dominated suspension. Continued decompression causes additional cracking of olivine that overprints earlier sealed cracks. These decompression events are expressed as the healed cracks; they trap inclusions and record melt and fluid compositions derived from the lower portion of the dyke thereby preserving the evolution in melt chemistry from early carbonatitic to late silicic olivine-saturated compositions (e.g., grey region; Fig. 7).

480 During formation of these later decompression cracks, the environment hosts a more
481 siliceous and, more hydrous, melt that is olivine saturated. This is indicated because the crack
482 healing involves both dissolution and crystallization of olivine to leave behind trails of mineral,
483 fluid and melt inclusions. This process is accelerated in a hydrous environment, which is
484 assumed here because hydrous phases are common in kimberlite and there is also a lack of
485 carbonate precipitation. The nature of the melt phase associated with the healed cracks is in
486 stark contrast to the CO_2-dominated fluid responsible for the carbonate filled sealed cracks. We
487 suggest this marks a time and space transition from the multiphase CO_2-rich fluid environment of
488 the dyke head to the denser, more siliceous, solids-rich kimberlite magma. The temporal (i.e.
489 late) restriction is imposed by the fact that there has to be a certain amount of Opx assimilation to
490 create a melt siliceous enough to saturate with olivine.
491

492 *8.3 Olivine saturation and crystallization*

493 The shapes of cores to xenocrystic and phenocrystic olivines are irregular to round in
494 shape (cf. Fedortchouk and Canil, 2004; Kamenetsky et al., 2008; Brett et al., 2009; Pilbeam et
495 al., 2013; Bussweiler et al., 2015; Sobolev et al., 2015), indicating a period of time when olivine
496 was reacting with the host melt and being dissolved. The result of this process is a population of
497 mantle-derived, xenocrystic olivines featuring highly varied but generally rounded and anhedral
498 shapes.

499 A consequence of orthopyroxene assimilation is that the original carbonatitic melt
500 becomes increasingly siliceous and magnesian in composition during ascent (Brett et al., 2009;
501 Russell et al., 2012, 2013; Pilbeam et al., 2013; Moussallem et al., 2014; Bussweiler et al., 2015).
502 With sufficient assimilation of Opx (and other silicate mantle minerals) the system can be driven
503 to olivine saturation (Brett et al., 2009; Kavanagh and Sparks, 2009; Russell et al., 2012; Pilbeam

et al., 2013). At this point the ascending magma is, for the first time, capable of crystallizing olivine. Olivine crystallization is expressed as overgrowths on the partially-corroded olivine xenocrysts and as microphenocrystic olivine in the groundmass. The healing of the late fractures in olivine involves dissolution and precipitation of the host mineral and is probably contemporaneous with olivine saturation.

We suggest that olivine crystallization occurs as modified olivine xenocrysts settle from the fluid-rich head of the dyke to the trailing solid-laden magma (Fig. 7). There, the surfaces of the olivine grains act as nucleation sites for both olivine crystallization and bubble nucleation allowing bubbles to be trapped as fluid inclusions on the interface between the core and the overgrowth (Fig. 3).

Olivine saturation and crystallization must occur after the carbonatitic melt has reached a putative kimberlitic composition (e.g., 15 to 20 wt. % SiO_2) requiring assimilation of ~15-20 wt. % Opx. We suggest that this chemical condition is only achieved at lower pressures, after the magma has transited most of the cratonic mantle lithosphere. Evidence supporting low pressure late crystallization of olivine in kimberlite derives from: (1) phase equilibria experiments in kimberlite (Canil and Bellis, 2008), (2) thermodynamic studies of adiabatic cooling during ascent predicting low pressure crystallization of olivine phenocrysts (Kavanagh and Sparks, 2009) and liberation of latent heat (Brett et al., 2009), and (3) olivine saturation estimates induced by orthopyroxene dissolution (< 60 km depth; Russell et al., 2012, 2013). However, the strongest evidence against high pressure, deep-seated crystallization of olivine is the fact that, at SiO_2 contents in excess of ~12 wt. %, clinopyroxene is a stable phase at pressures > 3 GPa (~90 km; e.g., Brey and Ryabchikov, 1994; Russell et al., 2013). In fact, as SiO_2 content approaches that of putative kimberlite, the pressure required to allow olivine crystallization and avoid clinopyroxene saturation is < 1 GPa (~30-35 km; cf. Fig. 11 of Luth, 2009).

Our study provides another line of evidence suggesting olivine saturation in kimberlite occurs late and shallow. Olivine crystallization produces overgrowths on partially corroded, sub-rounded olivine crystals that enclose both sealed and healed cracks. This marks a time and depth after which there was no further decompression cracking, otherwise decompression cracks would be visible in the overgrowths and in micro-phenocrysts. The saturation and crystallization of olivine can, therefore, only occur at depths less than ~25 km (Fig. 6b) from Earth's surface.

8.4 Milling Processes

Turbulent flow within the gas-rich region of the dyke suspends a multiphase (melt-gas-crystal) mixture and encourages rapid mechanical abrasion or milling of xenocrysts resulting in reshaping (i.e. rounding) and resurfacing (i.e. sandblasting) of xenocrystic material. We suggest that efficient milling of olivine xenocrysts by particle-particle interactions in a high velocity (i.e. turbulent) fluidized suspension of solids, melt and gas (e.g., Reid et al. 1975; Arndt et al., 2010) plays an important role throughout ascent. Initially, prior to olivine saturation, milling and chemical dissolution act to round olivine grains (Domains 2-4). The characteristic rough surfaces found on the olivine overgrowths indicate that milling processes also operate after olivine saturation is reached, after which, we suggest crystallization and mechanical milling are in constant competition. This competition is alluded to in Arndt et al. (2010) who described olivine macrocrysts having overgrowths of variable thicknesses and local stripping of overgrowths leaving only remnants preserved in depressions. The micron-scale roughness illustrated in Fig. 4C-E are characteristic of surfaces resulting from inelastic impacts and can be ascribed to ~25 micron-sized, semi-hemispherical chips caused by impacts with other solids (Jones et al., 2014).

Jet mills are an industrial analogue for the milling and rounding processes operating within the kimberlite dyke. Jet mills use high flow rates of solid and gas mixtures to efficiently

552 and rapidly produce narrow size distributions of rounded particles (Tuunila, 1997). Turbulent
553 flow of the fluidized suspension maximizes particle-particle collisions, which in turn accelerates
554 particle reshaping and resurfacing leading to rounded olivine grains (Dufek et al., 2012;
555 Campbell et al. 2013). Differential particle velocities govern the efficiency of, both, jet mill and
556 sand blasting processes. However, these processes also depend on high particle densities (cf. ash-
557 blasting of Campbell et al. 2013). It seems probable that, as mantle xenoliths are sampled and
558 disaggregated at the crack tip, the amount of mantle cargo will increase and the overall solid
559 particle density will rise. Increasing the particle density in the turbulent fluidized dyke head will
560 promote highly efficient milling leading to shape modification (25-33% mass loss from grains)
561 potentially operating on a timescale of minutes (Campbell et al., 2013; Jones et al., 2014).
562 The presence of mechanically rounded and milled olivine xenocrysts in kimberlite
563 constitutes very strong and the only direct evidence for the turbulent ascent of kimberlite.
564 Furthermore, as CO_2 volume increases (exsolution and expansion) during ascent, mechanical
565 milling is likely to become an increasingly efficient process. We argue that the rounded, pitted
566 and flaked olivine grains characterizing kimberlite (Figs. 4A-E) are produced late in the ascent,
567 at shallow (<25 km) depths by intense mechanical milling of olivine xenocrysts within a fluid-
568 dominated, turbulent multiphase magma.

569

570 **9. Summary**

571 Our model involves carbonatitic proto-kimberlite melts preferentially assimilating Opx
572 xenocrysts as they transit the cratonic mantle lithosphere to evolve into silicic-hydrous melts that
573 reach olivine saturation during ascent.

574 • Mantle-derived xenocrysts are supplied to the melt continuously by rapid disaggregation
575 of entrained mantle xenoliths (Domain 1; Fig. 7) due to decompression over path lengths
576 of 2-7 km (at > 0.5 m s^{-1}). The xenocrysts populate the fluid-filled turbulent dyke-tip
577 (Domain 2; Fig. 7).
578 • Efficient assimilation of Opx causes a drop in CO_2 solubility and spontaneous
579 effervescence of a CO_2-rich fluid in the deep mantle which increases buoyancy and
580 drives the melt towards SiO_2-enrichment.
581 • Rapid and accelerating ascent promotes decompression at increasing rates and olivine
582 grains fail in tension forming cracks (Domain 3; Fig. 7) over ascent distances of ~19 km.
583 Small wetting-angles between fluid and olivine allow infiltration of carbonate-melt that
584 seals the cracks.
585 • Olivine xenocrysts passed downwards from the gas-rich dyke head to the melt-rich dyke
586 tail. A later generation of decompression cracks in olivine, infiltrated by silicic melt and
587 fluid, form healed cracks that overprint carbonate-filled sealed cracks. (Domain 4; Figure
588 7).
589 • Opx assimilation by the carbonatitic melt results in a kimberlitic melt composition
590 leading to olivine saturation and crystallization at shallow (< 25 km) depths (Domain 4;
591 Fig. 7).
592 • At upper mantle depths, magma ascent accelerates due to increasing CO_2 fluid production
593 and expansion to create a fully fluidized, turbulent solids-rich melt suspension. High
594 energy particle-particle interactions promote efficient mechanical milling of the
595 xenocryst population causing their reshaping (rounding) and resurfacing (pitted and
596 flakey).

- Mantle cargo (xenocrysts and xenoliths) settles continuously through the melt column to accumulate at the base of the ascending kimberlite package. The crystal-rich tail of magma forms hypabyssal intrusions (Domain 5; Fig. 7) and effusive flows (IHV), or is left behind in the collapsed dyke within the mantle.

Acknowledgments

This research was funded by an NSERC Collaborative Research and Development Grant (Kimberlite eruption dynamics: Implications for diamond distribution in the Diavik kimberlite) held by JKR and sponsored by Diavik Diamond Mines, Inc. (DDM). GDMA was partly supported by NSF award HRD #1137774. We acknowledge critical and beneficial conversations with Tom McCandless, Barbara Scott Smith and Dan Marshall. Barry Hawthorne and Rich Brown are thanked for generously lending us kimberlite samples and thin sections, respectively, from the Igwisi Hills volcanoes. We were the beneficiaries of thorough reviews by Janine Kavanagh and Nick Arndt. We are particularly appreciative of Nick Arndt's substantive, critical, and fair review given our substantial but tantalizing differences in our respective interpretations.

Reference List

Arndt, N. T., Guitreau, M., Boullier, A.-M., Le Roex, A., Tommasi, A., Cordier, P. & Sobolev, A., 2010. Olivine and the origin of kimberlite. Journal of Petrology 51, 573-602.

Arndt, N.T., Boullier, A.M., Clement, J.P., Dubois, M., Schissel, D., 2006. What olivine, the neglected mineral, tells us about kimberlite petrogenesis. eEarth 1, 15–21.

Bodnar, R. J., 2003. Introduction to aqueous-electrolyte fluid inclusions. Fluid Inclusions: Analysis and Interpretation, 32, 81-100.

Brey, G. P., & Ryabchikov, I. D., 1994. Carbon-dioxide in strongly silica undersaturated melts and origin of kimberlite magmas. Neues Jahrbuch Fur Mineralogie-Monatshefte, (10), 449-463.

622 Brett, R. C., Russell, J. K., and Moss, S., 2009. Origin of olivine in kimberlite: Phenocryst or
623 imposter?: Lithos, v. 112, p. 201-212.
624 Brooker, R.A., Sparks, R.S.J., Kavanagh, J.L., Field, M. 2011. The volatile content of
625 hypabyssal kimberlite magmas: some constrains from experiments on natural rock
626 compositions.
627 Brown, R. J., Manya, S., Buisman, I., Fontana, G., Field, M., Mac Niocaill, C., Sparks, R.S.J.,
628 Stuart, F. M., 2012. Eruption of kimberlite magmas: physical volcanology,
629 geomorphology and age of the youngest kimberlitic volcanoes known on earth (the Upper
630 Pleistocene/Holocene Igwisi Hills volcanoes, Tanzania). Bulletin of volcanology, *74*(7),
631 1621-1643.
632 Bussweiler, Y., Foley, S. F., Prelević, D., Jacob, D. E., 2015. The olivine macrocryst problem:
633 New insights from minor and trace element compositions of olivine from Lac de Gras
634 kimberlites, Canada. *Lithos*, *220*, 238-252.
635 Campbell, M. E., Russell, J. K., & Porritt, L. A., 2013. Thermomechanical milling of accessory
636 lithics in volcanic conduits. Earth and Planetary Science Letters, 377, 276-286.
637 Canil, D., Bellis, A. J., 2008. Phase equilibria in a volatile-free kimberlite at 0.1 MPa and the
638 search for primary kimberlite magma. Lithos, 105(1), 111-117.
639 Clement C.R., Skinner, E.M., Scott Smith, B.H., 1984. Kimberlite Redefined. Journal of
640 Geology 92:223-228.
641 Cordier, C., Sauzeat, L., Arndt, N., Boullier, A., Batanova, V., Barou, F., 2015. Melt percolatioin
642 in the lithospheric mantle : insights form olivine xenocrysts in kimberlites. Journal of
643 Petrology. Accepted.
644 Dawson, J., 1994. Quaternary kimberlitic volcanism on the Tanzania Craton: Contributions to
645 Mineralogy and Petrology, v. 116, no. 4, p. 473-485.
646 Dufek, J., Manga, M., Patel, A., 2012. Granular disruption during explosive volcanic eruptions.
647 Nature Geoscience, 5(8), 561-564.
648 Fedortchouk, Y., Canil, D., 2004. Intensive variables in kimberlite magmas, Lac de Gras, Canada
649 and implications for diamond survival. Journal of Petrology, 45 1725-1745.
650 Griffin, W. L., O'Reilly, S. Y., Abe, N., Aulbach, S., Davies, R. M., Pearson, N., Doyle, B.,
651 Kivi, K., 2003. The origin and evolution of Archean lithospheric mantle. Precambrian
652 Research, 127(1), 19-41.
653 Jerram, D. A., Mock, A., Davis, G. R., Field, M., Brown, R. J., 2009. 3D crystal size

654 distributions: A case study on quantifying olivine populations in kimberlites. Lithos, 112,
655 223-235.
656 Jones, T. J., Russell, J. K., Porritt, L. A., and Brown, R. J., 2014. Morphology and surface
657 features of olivine in kimberlite: implications for ascent processes, Solid Earth, 5, 313-
658 326, doi:10.5194/se-5-313-2014..
659 Kamenetsky, V. S., Kamenetsky, M. B., Sobolev, A. V., Golovin, A. V., Demouchy, S., Faure,
660 K., Sharygin, V. V., and Kuzmin, D. V., 2008. Olivine in the Udachnaya-East kimberlite
661 (Yakutia, Russia): types, compositions and origins. Journal of Petrology, v. 49, no. 4, p.
662 823-839.
663 Kamenetsky, V. S., Grütter, H., Kamenetsky, M. B., Gömann, K., 2013. Parental carbonatitic
664 melt of the Koala kimberlite (Canada): Constraints from melt inclusions in olivine and
665 Cr-spinel, and groundmass carbonate. Chemical Geology, 353, 96-111.
666 Kamenetsky, V. S., Yaxley, G. M., 2015. Carbonate-silicate liquid immiscibility in the mantle
667 propels kimberlite magma ascent. Geochemica et Cosmochimica, 158, 48-56.
668 Kavanagh, J. L., Menand, T., Sparks, R. S. J., 2006. An experimental investigation of sill
669 formation and propagation in layered elastic media. Earth and Planetary Science
670 Letters, 245(3), 799-813.
671 Kavanagh, J. L., Sparks, R. S. J., 2009. Temperature changes in ascending kimberlite magma.
672 Earth and Planetary Science Letters, 286(3), 404-413.
673 Kavanagh, J. L., Sparks, R. S. J., 2011. Insights of dyke emplacement mechanics from detailed
674 3D dyke thickness datasets. Journal of the Geological Society, 168(4), 965-978.
675 Lensky, N. G., Niebo, R. W., Holloway, J. R., Lyakhovsky, V., Navon, O., 2006. Bubble
676 nucleation as a trigger for xenolith entrapment in mantle melts: Earth and Planetary
677 Science Letters, v. 245, no. 1-2, p. 278.
678 Luth, R. W., 2009. The activity of silica in kimberlites, revisited. Contributions to Mineralogy
679 and Petrology, 158(2), 283-294.
680 McGetchin, T. R., Ullrich, G. W., 1973. Xenoliths in maars and diatremes with inferences for the
681 Moon, Mars, and Venus. Journal of geophysical research, 78(11), 1833-1853.
682 Menand, T., Tait, S. R., 2002. The propagation of a buoyant liquid-filled fissure from a source
683 under constant pressure: An experimental approach. Journal of Geophysical Research:
684 Solid Earth (1978–2012), 107(B11), ECV-16.

685 Mercier, J. C. C., 1979. Peridotite xenoliths and the dynamics of kimberlite intrusion. The
686 Mantle Sample: Inclusion in Kimberlites and Other Volcanics, 197-212.
687 Mitchell, R. H., 1973. Composition of olivine, silica activity and oxygen fugacity in kimberlite:
688 Lithos, v. 6, p. 65-81.
689 Mitchell, R. H., 1986. Kimberlites: Mineralogy, Geochemistry and Petrology.
690 Moss, S., Russell, J. K., Brett, R. C., Andrews, G. D. M., 2009. Spatial and temporal evolution of
691 kimberlite magma at A154N, Diavik, Northwest Territories, Canada. Lithos, 112, 541-
692 552.
693 Moss, S., Russell, J. K., Smith, B. H. S., Brett, R. C., 2010. Olivine crystal size distributions in
694 kimberlite: American Mineralogist, v. 95, no. 4, p. 527-536.
695 Moussallem, Y., Morizet, Y., Massuyeau, M., Laumonier, M., and Gaillard, F., 2014.
696 CO_2 Solubility in Kimberlite melts. Chemical Geology.
697 Patterson, M., Francis, D., McCandless, T., 2009. Kimberlites: Magmas or mixtures? Lithos,
698 112, 191-200.
699 Pilbeam, L. H., Nielsen, T., and Waight, T. E., 2013. Digestion fractional crystallization (DFC):
700 an important process in the genesis of kimberlites. Evidence from olivine in the Majuagaa
701 kimberlite, southern West Greenland: Journal of Petrology, v. 54, no. 7, p. 1399-1425.
702 Reid, A. M., Donaldson, C., Dawson, J., Brown, R., and Ridley, W., 1975. The Igwisi Hills
703 extrusive "kimberlites": Physics and Chemistry of the Earth, v. 9, p. 199-218.
704 Roedder, E., 1984. Fluid Inclusions; Reviews in Mineralogy In Mineralogical Society of
705 America.
706 Russell, J.K., Porritt, L., Lavallee, Y., Dingwell, D., 2012. Kimberlite ascent by assimilation-
707 fuelled buoyancy. Nature 481, 352–356.
708 Russell, J.K., Porritt, L., Hilchie, L., 2013. Kimberlite: Rapid ascent of lithospherically modified
709 carbonatites. Journal Geological Society India. Special Issue from Proceedings of 10th
710 International Kimberlite Conference, (D. G. Pearson et al. (eds.), **1**, 195-210. (DOI:
711 10.1007/978-81-322-1170-9_12)
712 Rubin, A. M., 1995. Propagation of magma-filled cracks. Annual Review of Earth and Planetary
713 Sciences, 23, 287-336.
714 Smith, D.L., Evans, B., 1984. Diffusional crack healing in quartz. J. Geophys. Res., 89, 4125-
715 4135.
716 Sobolev, N. V., 1977. Deep-Seated Inclusions in Kimberlites and the Problem of the
717 Composition of the Upper Mantle (Vol. 11, pp. 1-279). American Geophysical Union.

718 Sobolev, N. V., Sobolev, A. V., Tomilenko, A. A., Kovyazin, S. V., Batanova, V. G., Kuz'min,
719 D. V., 2015. Paragenesis and complex zoning of olivine macrocrysts from unaltered
720 kimberlite of the Udachnaya-East pipe, Yakutia: relationship with the kimberlite
721 formation conditions and evolution. *Russian Geology and Geophysics*, *56*(1), 260-279.
722 Sparks, R. S. J., Baker, L., Brown, R. J., Field, M., Schumacher, J., Stripp, G., Walters, A., 2006.
723 Dynamical constraints on kimberlite volcanism: Journal of Volcanology and Geothermal
724 Research, v. 155, no. 1-2, p. 18-48.
725 Sparks, R. S. J., 2013. Kimberlite volcanism. Annual Review of Earth and Planetary Sciences,
726 41, 497-528.
727 Tuunila, R., 1997. Ultrafine grinding of FGD and phosphogypsum with an attrition bead mill and
728 a jet mill. Ph.D. Thesis, Lappeenranta University of Technology.
729 Vergniolle, S., Jaupart, C., 1986. Separated two-phase flow and basaltic eruptions. Journal of
730 Geophysical Research: Solid Earth (1978–2012), 91(B12), 12842-12860.
731 Wanamaker, B. J., Wong, T.F., Evans, B., 1990. Decrepitation and crack healing of fluid
732 inclusions in San Carlos olivine. J. Geophys. Res., 95(B10), 15,623–15,641.
733 Wilson, L., Head, J. W., 2007. An integrated model of kimberlite ascent and eruption: Nature, v.
734 447, no. 7140, p. 53-57.
735

Typeset, published version: https://doi.org/10.1016/j.epsl.2015.05.024

Figure Captions

Fig. 1. Photomicrographs of three classes of olivine hosted by kimberlite. (A-B) xenocrystic olivine (macrocrysts) with distinct rims formed by overgrowths of olivine. (C-D) smaller (~200 μm), phenocryst-like, olivines comprising core of rounded olivine xenocryst and euhedral rim of olivine overgrowth. (E) Neoblastic growth within a strained olivine xenocryst (crossed-nicols image; xpl), (F) Neoblastic growth overprinting crack networks (plane-polarized light; ppl). Samples are from Diavik (A, C, E) and Igwisi Hills (B, D, F).

Fig. 2. Photomicrographs showing occurrences of sealed cracks in olivine xenocrysts from Diavik, N.W.T., Canada. (A) Crossed-nicols (xpl) image of olivine (Ol) xenocryst at extinction illustrating a network of sub-parallel, carbonate-filled, sealed cracks. (B) Back-scattered electron (BSE) image of carbonate-sealed crack within olivine (Sr-cc; Sr-rich calcite). (C) Photomicrograph under plane-polarized light (ppl) showing sealed crack terminating at the interface between the original rounded olivine and its olivine overgrowth (rim). (D) BSE image of carbonate-sealed cracks contained within a xenocrystic core of olivine (darker grey) and bounded by an overgrowth of olivine having lower forsterite content (lighter grey).

Fig. 3. Photomicrographs of healed cracks within olivine xenocrysts. (A) Healed crack within olivine from Diavik kimberlite defined by a trail of residual fluid inclusions; crack terminates against the olivine overgrowth. Inset shows networks of healed fractures (dark bands) within a single xenocryst. (B) Photomicrograph of an olivine xenocryst from Igwisi Hills showing the distribution of healed cracks defined by discontinuous trails of fluid inclusions; inset shows in intense network of healed cracks within the entire grain. (C) Interconnected dendritic networks of inclusions; (D) long irregular vermicular inclusions; and (E) smaller equant, rounded to crystal-shaped, isolated inclusions. (F) false coloured BSE image of a cracked olivine macrocryst showing an irregular shaped core cut by several healed cracks; olivine overgrowth (i.e. rim) and olivine near the crack have lower forsterite contents (lighter red) than the host crystal (darker red), (G) Magnified view of olivine xenocryst showing crosscutting relationship between earlier formed sealed crack and later cross-cutting healed fracture.

767 **Fig. 4**. Photomicrographs illustrating shapes and surfaces of olivine xenocrysts in kimberlite.
768 (A) Photomicrograph (ppl) of abundant rounded and ellipsoidal olivine within the Igwisi Hills
769 lava (B) Photomicrograph (xpl) of subrounded olivine grains from Diavik kimberlite (C) SEM
770 image of well-rounded olivine xenocryst from Igwisi Hills showing surface characterized by
771 micro-flaking and pitting. (D) SEM image of olivine grain separated from Diavik coherent
772 kimberlite, showing the well-rounded, sub-spherical 3D geometry. (E) Typical surface of
773 kimberlitic olivine within IH lava. The spherical surfaces characteristic of both IH and Diavik
774 olivine are rough at the micron scale due to micro-flaking and pitting. (F) Smooth primary
775 surfaces of olivine within a mantle-derived peridotite; smooth surfaces and sharp planar
776 intergranular contacts reflect textural equilibration at mantle conditions.
777
778 **Fig. 5**. Schematic representation of the "*kimberlite factory*". (A) The kimberlite factory
779 comprises a set of processes: 1) cracking of the overlying mantle lithosphere; 2) propagation and
780 episodic advance of the fluid-wetted crack-tip; 3) sampling and entrainment of mantle wall
781 rocks; 4) ascent of the kimberlite and inflation of a new length of dyke; and 5) elastic recovery
782 and closing up of tail of the kimberlite dyke. These processes are repeated continuously as the
783 factory moves progressively through the mantle lithosphere. (B) A schematic image of the
784 multiphase-multi-flow architecture within the kimberlite factory. The factory is an elastically-
785 inflated bulbous portion of the kimberlite dyke head having minimum critical width (W_c) and
786 length (L_c). The upper portion of the factory (white region) comprises a turbulent, CO_2-rich
787 fluid-dominated suspension of olivine xenocrysts. The olivine xenocrysts derive from
788 disaggregation of mantle xenoliths sampled in the damage zone formed at the crack-tip. Below
789 this zone (grey region) is a transitional flow regime comprising frothy kimberlite melt and
790 xenoliths and xenocrysts settled out of the overlying turbulent column of fluid.
791
792 **Fig. 6**. Model for crack formation within kimberlite-hosted olivine xenocrysts due to
793 decompression. (A) Schematic representation of increasing internal stresses ($\Delta\sigma$) within olivine
794 xenocrysts driven by rapid depressurization attending kimberlite ascent. Internal elastic stresses
795 build up linearly (positive values of $\Delta\sigma$) with increasing transport distance whereas the viscous
796 dissipation of internal stresses depends on ascent rate and transport distance (curvilinear lines
797 negative values of $\Delta\sigma$). (B) Calculated residual internal stresses due to rapid decompression are
798 plotted *vs*. transport distance from source at several ascent rates (solid curves). The heavy dashed

799 line marks the ascent rate-distance coordinates where viscous relaxation begins to dominate over
800 internal elastic stresses caused by depressurization. Also shown are tensile strengths for coarse-
801 (CG) and fine-grained (FG) peridotitic xenoliths. Dashed grey line is an infeasible extension
802 where the potential magnitude of viscous relaxation is greater than the internal elastic stresses.
803
804 **Fig. 7**. Schematic diagram of the linkages (1-5) between observed textural properties of olivine
805 and processes operating within the kimberlite factory. From the inflated crack-tip front to the
806 relaxed trailing dyke region of the factory, the domains include: 1) sampling of mantle wall
807 rocks; 2) concomitant decompression cracking and milling of olivine xenocrysts in a turbulent
808 streaming suspension of CO_2-rich fluid; 3) sedimentation and re-entrainment of milled olivines
809 into melt-dominated portion of kimberlite; 4) minor heterogeneous crystallization of olivine on
810 milled and rounded xenocrysts in relatively degassed kimberlite; and 5) continued settling and
811 passage of olivine sediment through the gas-depleted tail of the kimberlite. The kimberlite melt
812 continues to supply exsolved fluid to the overlying suspension and collect olivine xenocrysts
813 which settle continuously to the trailing magma-filled, collapsed dyke which is solids-enriched.
814

Table 1. Summary of variables and parameters used to model decompression cracking of olivine xenocrysts during ascent.

Symbol	Units	Description	Value[1]
$\Delta\sigma_R$	Pa	Residual internal stress	
$\Delta\sigma_E$	Pa	Elastic stress	
$\Delta\sigma_V$	Pa	Viscous stress dissipation	
P_o	Pa	Confining pressure	
z_o	m	Initial depth	190 km
U	m s^{-1}	Ascent velocity	0.1 to >1
ρ	kg m^{-3}	Mantle density	3300
K	Pa	Bulk modulus (at 1300 ^oC)	~$1.4x10^{11}$
η	Pa s	Viscosity of OH-rich olivine	10^{17}
σ_{Ol}	MPa	Tensile strength of olivine	500
σ_{fx}	MPa	Xenolith strength (fine)	200
σ_{cx}	MPa	Xenolith strength (coarse)	100

[1]Sources given in Supplementary Appendix B.

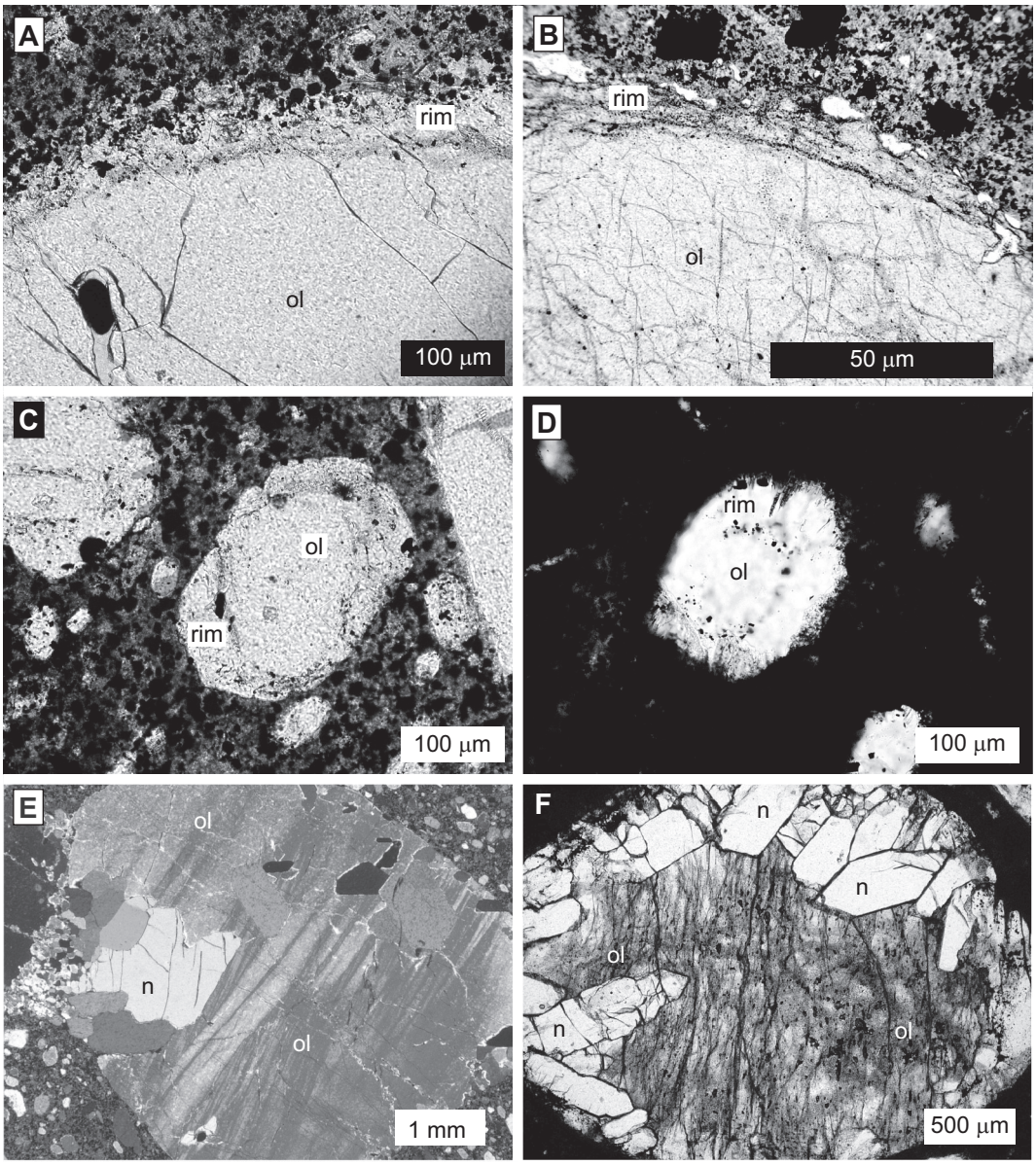

Fig 1 Brett 2015
1.5 column width

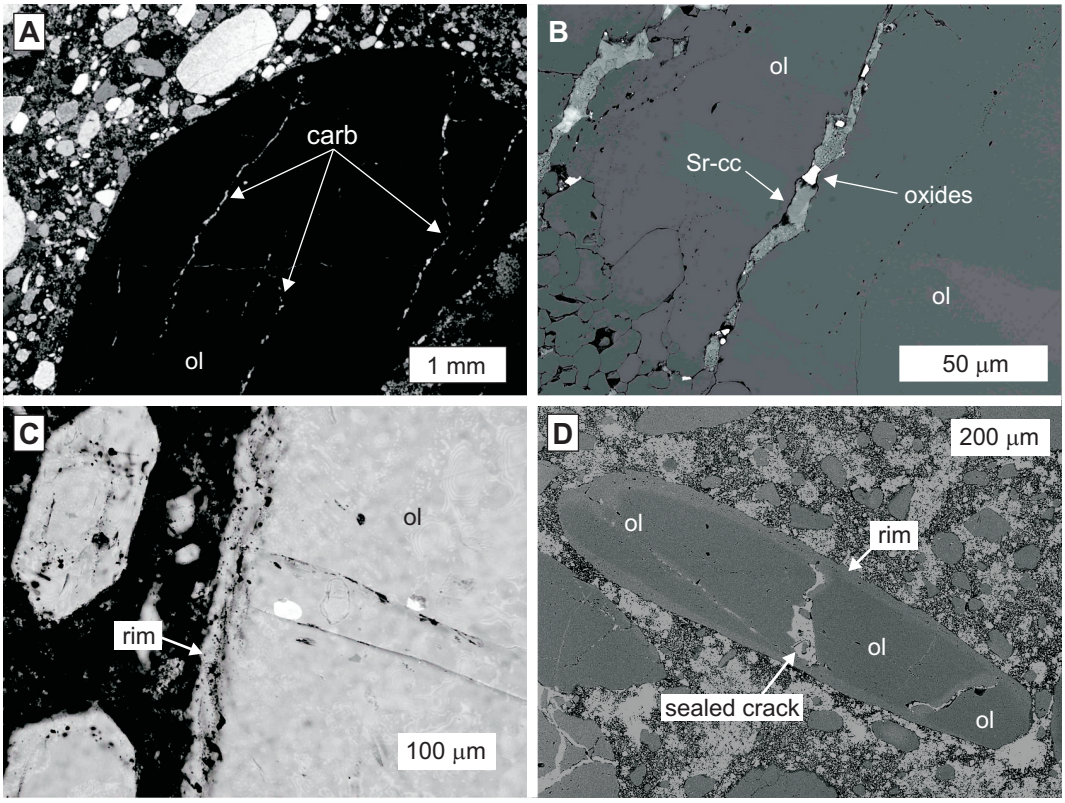

Fig 2 Brett 2015
1.5 column width

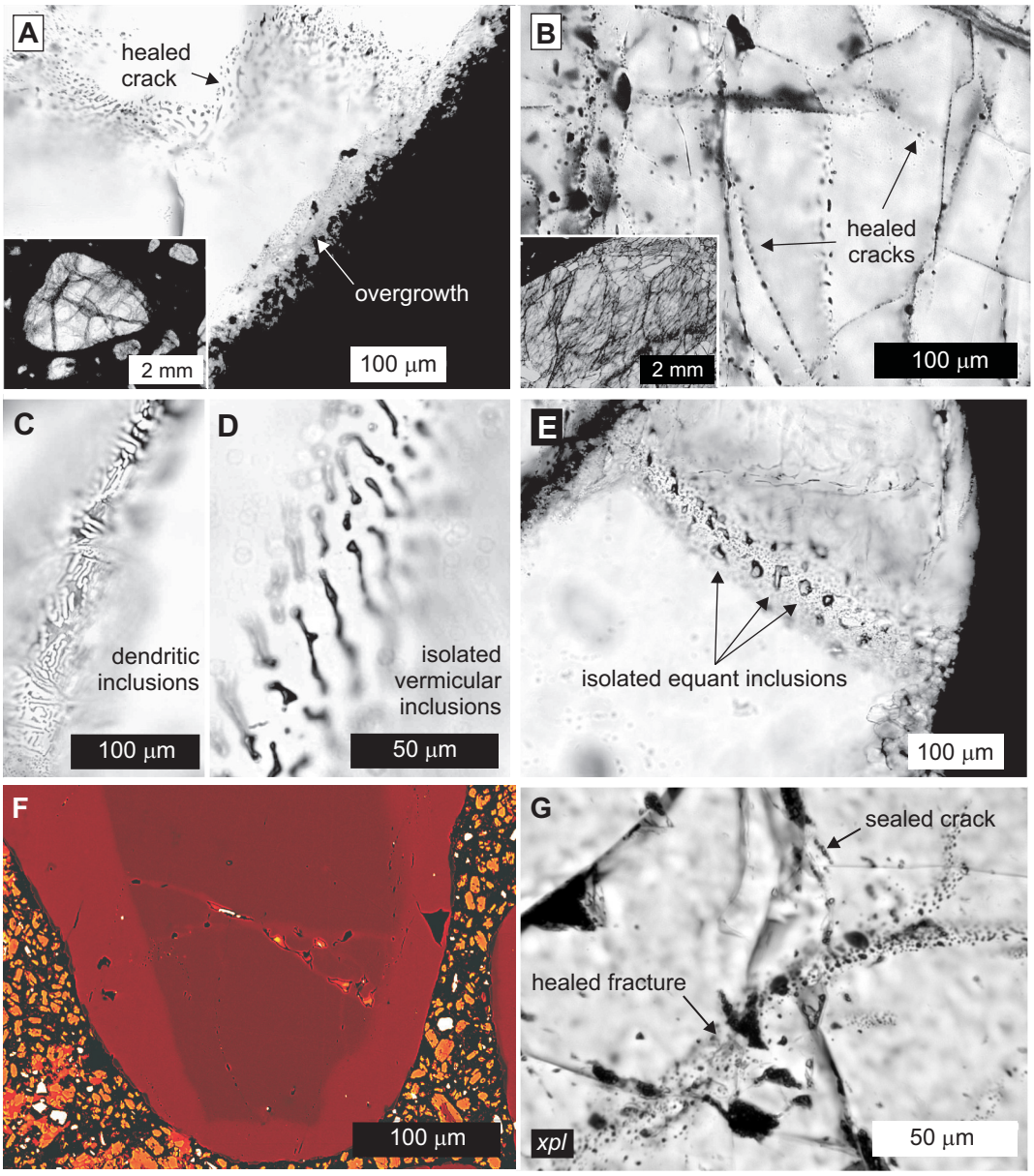

Fig 3 Brett 2015
1.5 column width

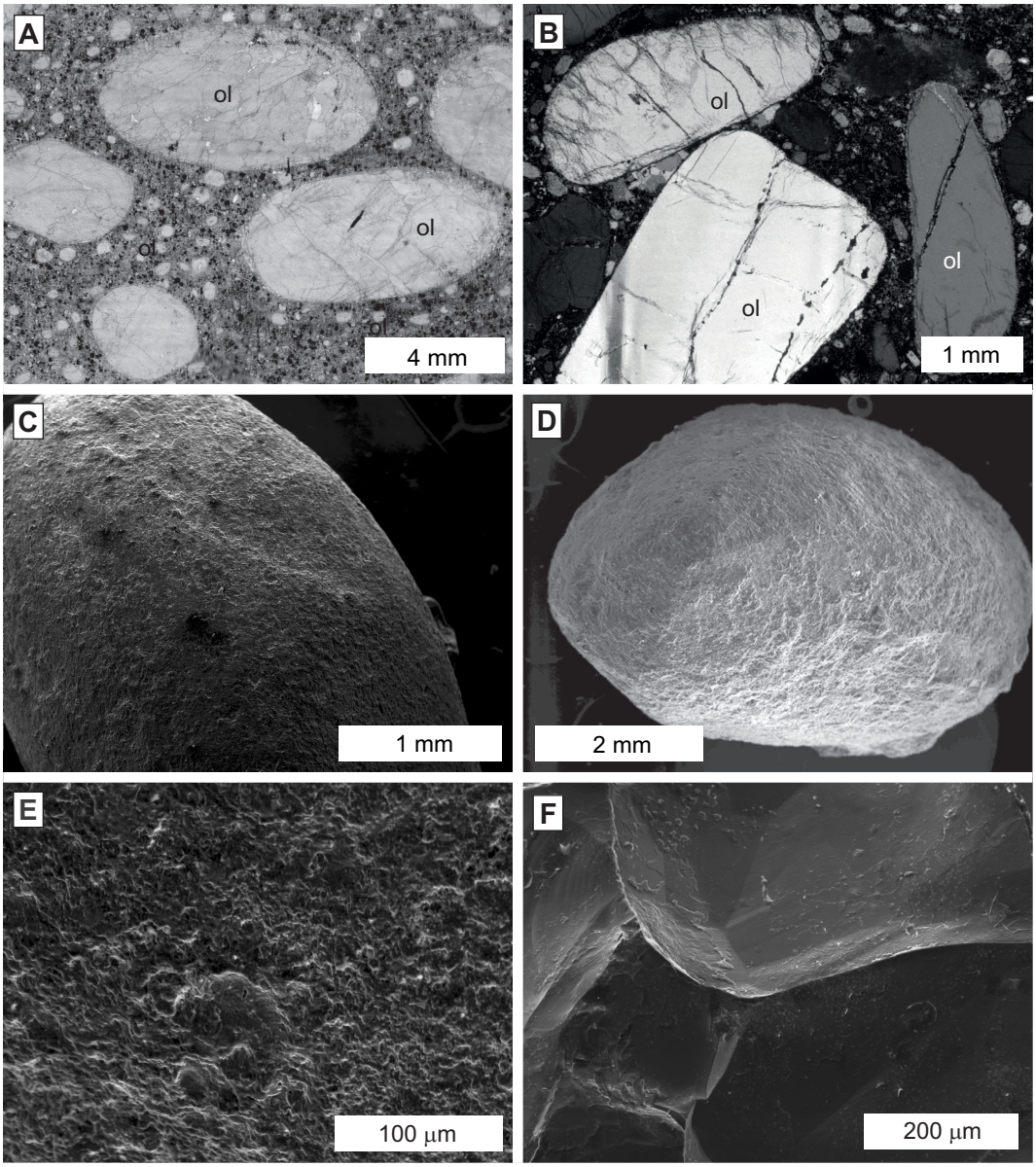

Fig 4 Brett 2015
1.5 column width

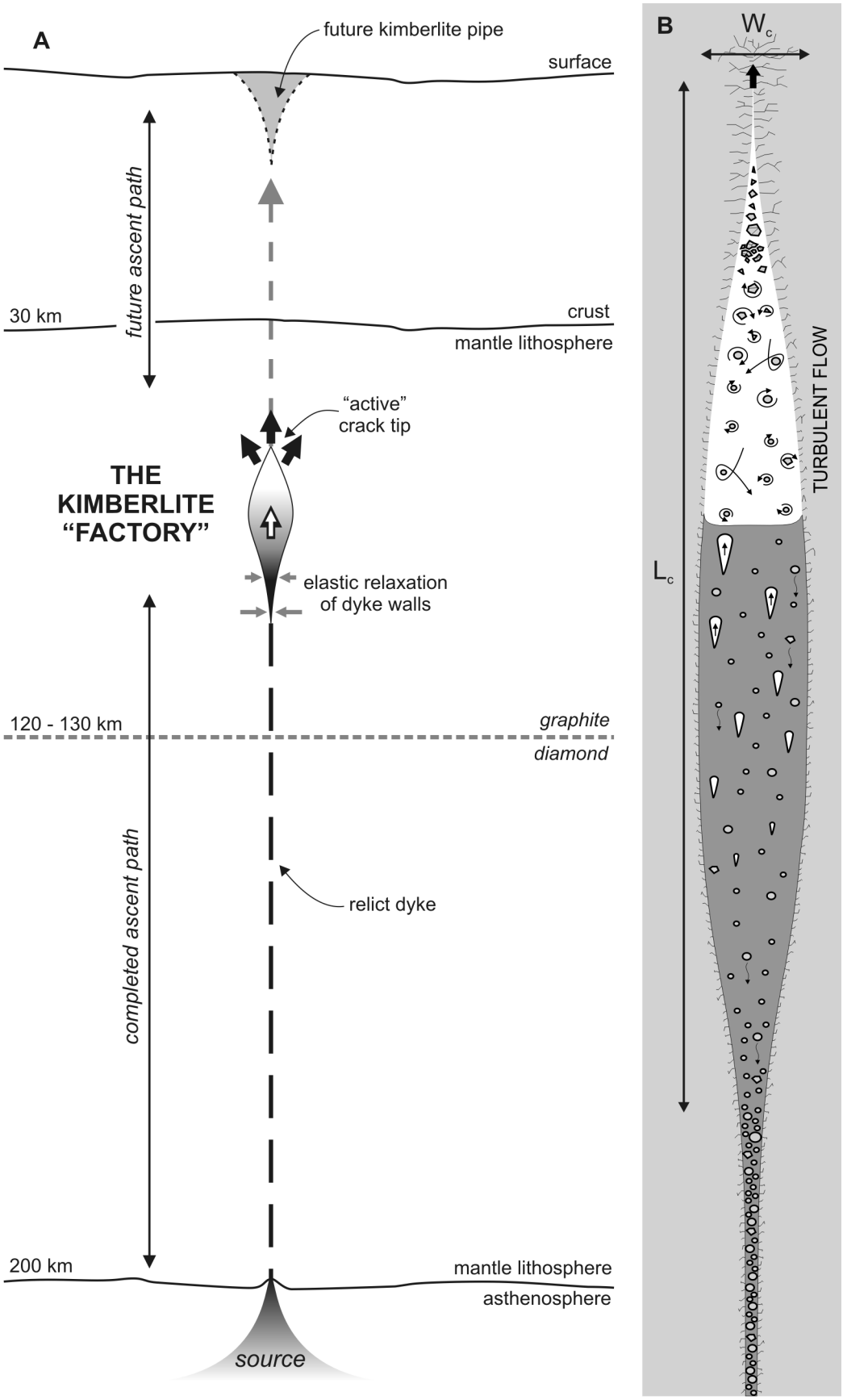

Fig 5 Brett 2015
1.5 column width

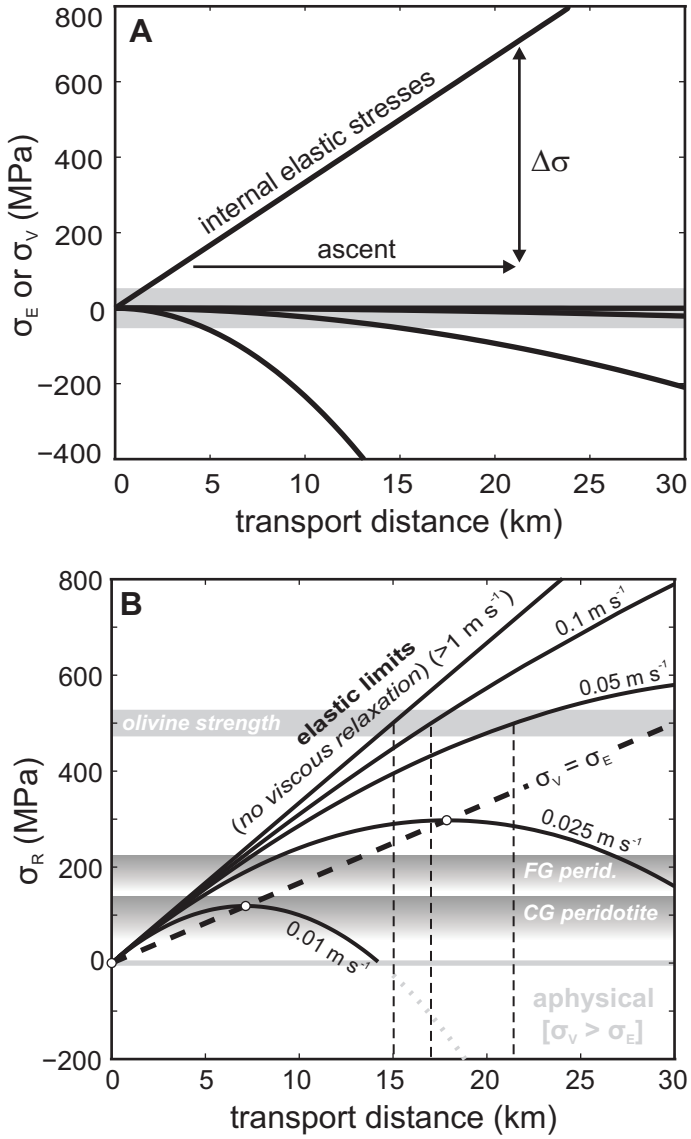

Fig 6 Brett 2015
single column width

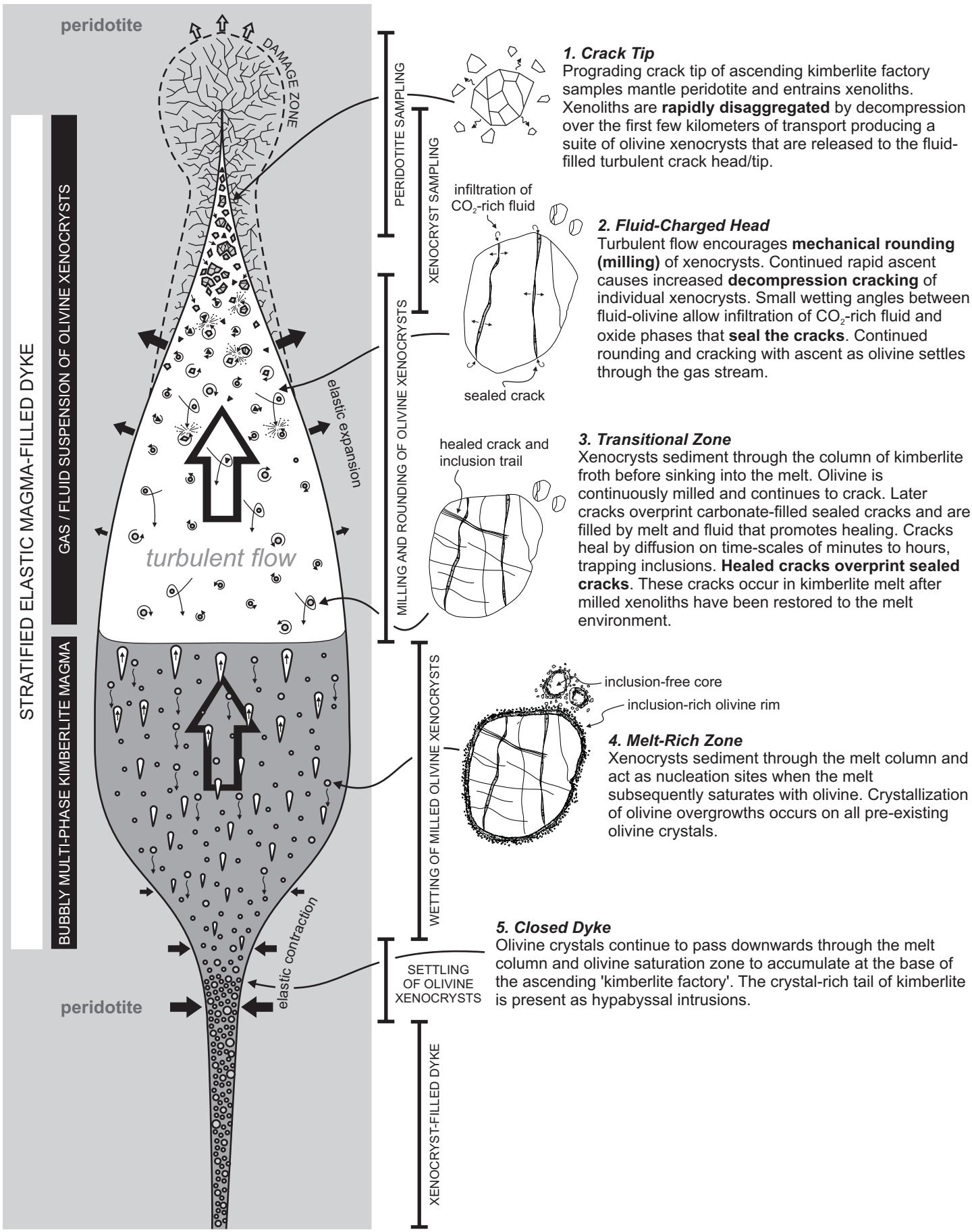

1. Crack Tip
Prograding crack tip of ascending kimberlite factory samples mantle peridotite and entrains xenoliths. Xenoliths are **rapidly disaggregated** by decompression over the first few kilometers of transport producing a suite of olivine xenocrysts that are released to the fluid-filled turbulent crack head/tip.

2. Fluid-Charged Head
Turbulent flow encourages **mechanical rounding (milling)** of xenocrysts. Continued rapid ascent causes increased **decompression cracking** of individual xenocrysts. Small wetting angles between fluid-olivine allow infiltration of CO_2-rich fluid and oxide phases that **seal the cracks**. Continued rounding and cracking with ascent as olivine settles through the gas stream.

3. Transitional Zone
Xenocrysts sediment through the column of kimberlite froth before sinking into the melt. Olivine is continuously milled and continues to crack. Later cracks overprint carbonate-filled sealed cracks and are filled by melt and fluid that promotes healing. Cracks heal by diffusion on time-scales of minutes to hours, trapping inclusions. **Healed cracks overprint sealed cracks**. These cracks occur in kimberlite melt after milled xenoliths have been restored to the melt environment.

4. Melt-Rich Zone
Xenocrysts sediment through the melt column and act as nucleation sites when the melt subsequently saturates with olivine. Crystallization of olivine overgrowths occurs on all pre-existing olivine crystals.

5. Closed Dyke
Olivine crystals continue to pass downwards through the melt column and olivine saturation zone to accumulate at the base of the ascending 'kimberlite factory'. The crystal-rich tail of kimberlite is present as hypabyssal intrusions.

Figure 7. Brett 2015